A penalty immersed boundary method for a rigid body in fluid

Cite as: Phys. Fluids **28**, 033603 (2016); https://doi.org/10.1063/1.4944565
Submitted: 16 November 2015 . Accepted: 05 March 2016 . Published Online: 30 March 2016

Yongsam Kim, and Charles S. Peskin

PHYSICS OF FLUIDS **28**, 033603 (2016)

A penalty immersed boundary method for a rigid body in fluid

Yongsam Kim[1,a)] and Charles S. Peskin[2,b)]
[1]*Department of Mathematics, Chung-Ang University, Dongjakgu Heukseokdong, Seoul 156-756, South Korea*
[2]*Courant Institute of Mathematical Sciences, New York University, 251 Mercer Street, New York, New York 10012, USA*

(Received 16 November 2015; accepted 5 March 2016; published online 30 March 2016)

We extend the penalty immersed boundary (pIB) method to the interaction between a rigid body and a surrounding fluid. The pIB method is based on the idea of splitting an immersed boundary, which here is a rigid body, notionally into two Lagrangian components: one is a massive component carrying all mass of the rigid body and the other is massless. These two components are connected by a system of stiff springs with 0 rest length. The massless component interacts with the surrounding fluid: it moves at the local fluid velocity and exerts force locally on the fluid. The massive component has no direct interaction with the surrounding fluid and behaves as though in a vacuum, following the dynamics of a rigid body, in which the acting forces and torques are generated from the system of stiff springs that connects the two Lagrangian components. We verify the pIB method by computing the drag coefficients of a cylinder and ball descending though a fluid under the influence of gravity and also by studying the interaction of two such descending cylinders and likewise the interaction of two such descending balls. The computational results are quite comparable to those in the literature. As a further example of an application, we include a freely falling maple seed with autorotation. © *2016 AIP Publishing LLC.* [http://dx.doi.org/10.1063/1.4944565]

I. INTRODUCTION

We extend the penalty immersed boundary (pIB) method to simulate the interaction between a rigid body and a surrounding fluid. The immersed boundary (IB) method has been widely used to investigate the problems in which an elastic boundary or body is immersed in and interacts with a surrounding fluid.[1–3] Kim and Peskin[4] have introduced an extension of the IB method which can easily deal with an elastic boundary with mass. We call it the pIB method and have shown in Ref. 4 that the pIB method can solve many problems in which mass of the immersed boundary plays an important dynamical role. For more examples of the application of the pIB method, see Refs. 5–7. One advantage of the pIB method is that its numerical implementation is a simple modification of the framework of an existing IB method code for the massless case.

The pIB method is based on the idea of splitting an immersed boundary notionally into two Lagrangian components: one is a massive component carrying all mass of the boundary and the other is massless. These two components are connected by a system of stiff springs with 0 rest length. The massless component interacts with the surrounding fluid: it moves at the local fluid velocity and exerts force locally on the fluid. The massive component has *no* direct interaction with the fluid and behaves as though in a vacuum, following Newton's law of motion, in which the only forces that appear are the force of the springs that connect the two Lagrangian components and the gravitational force acting on the massive component. As the stiffness of the springs that

a)Electronic mail: kimy@cau.ac.kr. Telephone: 82.2.820.5219. Fax: 82.2.820.5214.
b)Electronic mail: peskin@cims.nyu.edu. Telephone: 212.998.3126. Fax: 212.995.4121.

link the massless component to the massive component goes to infinity, the massive component accompanies the massless component and provides it with mass. For the quantitative verification of this behavior, see Ref. 4.

Using the same idea of the pIB method, we introduce two representations for a rigid body: a massless component and a massive component which are connected by stiff springs. The massless component moves at the local fluid velocity and exerts force locally to the fluid. The force that it applies to the fluid is the force generated from the stiff springs that link it to its massive counterpart. On the other end of the spring, the massive component moves as though in a vacuum following the dynamics of a rigid body in which forces and torques acting on the massive component are the gravitational force and those generated from the springs that connect it to the massless counterpart.

In the pIB method, we separate the dynamics of a rigid body only through a system of stiff springs from the whole system that, otherwise, would strongly couple the rigid body dynamics to the fluid dynamics through constraints. By doing that, we allow the equations for the fluid motion itself to be as simple as possible. Particularly, we keep the density of the fluid equations to be uniformly constant. This idea of uncoupling a given dynamical system using a penalty parameter has also been used in the immersed boundary-lattice Boltzmann method[8,9] in which the fluid equations are solved using lattice Boltzmann method to simulate the sedimentation of rigid bodies.

There has been a considerable amount of work done on the design of numerical methods to provide an accurate computational tool for the interaction between fluid and rigid bodies. Arbitrary Lagrangian-Eulerian (ALE) schemes have been successfully employed for direct simulations of fluid-solid systems.[10,11] Coquerelle and Cottet introduced a vortex method for the simulation of the interaction of an incompressible flow with rigid bodies.[12] A Lagrange-multiplier-based fictitious-domain method (DLM) for the direct numerical simulation of rigid particulate flows in a Newtonian fluid has also been used extensively.[13–15]

The IB method, but with a different way of enforcing the rigid-body constraint from the one described here, has also been applied for rigid body motions in an incompressible Navier-Stokes flow.[16–21] The authors in Ref. 17 give the mass effect of the immersed body by using the Boussinesq approximation which can be applied only for low Reynolds number flows with an extremely small added mass. Also they construct a mechanical model for the rigid body using a network of stiff springs which generate spring forces to enforce the rigidity of the immersed body.[17,18] These spring forces for the mechanical model and the penalty force of our method are different, but they both lead to numerical stiffness which requires very small time steps when these forces are explicitly handled. A number of direct forcing IB methods[19–21] also have been developed which use the body force computed directly from the governing equations so as to satisfy the no-slip boundary conditions exactly on the rigid body. Whereas these methods avoid the severe time step restriction arising from very stiff springs, they are considerably more complicated to implement, especially when the immersed body is moving.

In order to verify that the present pIB method is a robust and efficient numerical technique to simulate a rigid body interacting with a surrounding fluid, we simulate a well-known benchmark problem: a freely falling cylinder. In this test, we compare drag coefficients obtained by our numerical simulation with the experimental data in Ref. 22 and perform a convergence study, which shows that the pIB method is first-order accurate. The interaction between two cylinders falling in a fluid-filled channel is investigated. We also simulate the sedimentation of a single sphere and the interaction of two falling spheres in 3D flow. Finally we apply the pIB method to the simulation of the rotational motion of a falling maple seed. Our simulation results on the descent rate, the speed of rotation, and the coning angle, which characterize the autorotation of a maple seed, agree well with those obtained experimentally[23] and numerically using another method.[18] In fact, the method used in Ref. 18 was the original pIB method, so it was necessary there to construct a mechanical model of the maple seed. Here, we just use the rigid-body constraint.

II. EQUATIONS OF MOTION

Consider a 3D viscous incompressible fluid containing a rigid body. In the pIB method, we use two Lagrangian descriptions of the immersed body. One of its descriptions, denoted $\mathbf{X}(q,r,s,t)$ where (q,r,s) are curvilinear coordinates and t is time, has no mass and plays the same role as an immersed boundary in a more traditional IB method with massless boundary assumption. The other description, which we denote $\mathbf{Y}(q,r,s,t)$, carries all of the excess mass and is connected to $\mathbf{X}(q,r,s,t)$ by a system of stiff springs. The excess mass is the difference between the mass of the body and the mass of the fluid it displaces. The different points of the massive boundary have no direct connection to the fluid and move together as though a rigid body in a vacuum, with the only forces and torques applied on the body being the force of gravity and those generated from the springs that connect the massless description to the massive description of the rigid body.

Then the equations of the motion for a 3D viscous incompressible fluid interacting with an immersed body are the following:

$$\rho\left(\frac{\partial \mathbf{u}}{\partial t} + \mathbf{u}\cdot\nabla\mathbf{u}\right) = -\nabla p + \mu\Delta\mathbf{u} + \mathbf{f}, \tag{1}$$

$$\nabla\cdot\mathbf{u} = 0, \tag{2}$$

$$\mathbf{F}(q,r,s,t) = K(\mathbf{Y}(q,r,s,t) - \mathbf{X}(q,r,s,t)), \tag{3}$$

$$\mathbf{f}(\mathbf{x},t) = \int \mathbf{F}(q,r,s,t)\delta(\mathbf{x} - \mathbf{X}(q,r,s,t))dqdrds, \tag{4}$$

$$\frac{\partial \mathbf{X}}{\partial t}(q,r,s,t) = \mathbf{u}(\mathbf{X}(q,r,s,t),t) = \int \mathbf{u}(\mathbf{x},t)\delta(\mathbf{x} - \mathbf{X}(q,r,s,t))d\mathbf{x}. \tag{5}$$

The equations of motion of the rigid body itself will be given later.

Eqs. (1) and (2) are the Navier-Stokes equations for a viscous incompressible fluid in which the parameters ρ and μ are constant representing the fluid density and viscosity, respectively. The unknowns in the Navier-Stokes equations are the velocity field, $\mathbf{u}(\mathbf{x},t)$; the fluid pressure, $p(\mathbf{x},t)$; and the external force per unit volume applied by the immersed body $\mathbf{X}(q,r,s,t)$ to the fluid, $\mathbf{f}(\mathbf{x},t)$. Here t is the time, and $\mathbf{x} = (x,y,z)$ are the Cartesian coordinates. Note that the domain on which the Navier-Stokes equations (1) and (2) are defined includes the domain occupied by the rigid body. In the IB method, there is always fluid everywhere. Anything immersed in the fluid is regarded as a part of the fluid in which forces are applied and in which additional mass may be present.

Eq. (3) defines the force density $\mathbf{F}$ which is applied by the massless component $\mathbf{X}(q,r,s,t)$ of the immersed body to the fluid so that $\mathbf{F}(q,r,s,t)dqdrds$ is the force transmitted to the fluid by the volume element $dqdrds$ of the body. The force density $\mathbf{F}$ is generated by the stiff springs that connect the massive and massless descriptions of the immersed body. As the stiffness parameter K, which is called the "penalty" parameter of the method, gets large, the energy penalty increases that must be paid to separate the two descriptions $\mathbf{Y}(q,r,s,t)$ and $\mathbf{X}(q,r,s,t)$ by any given amount. We shall discuss below the case in which $K \to \infty$.

The interaction Equations (4) and (5) express the local character of the interaction through the three-dimensional Dirac delta function $\delta(\mathbf{x}) = \delta(x)\delta(y)\delta(z)$. Eq. (4) relates the two corresponding force densities $\mathbf{f}(\mathbf{x},t)d\mathbf{x}$ and $\mathbf{F}(q,r,s,t)dqdrds$, which can been seen by integrating each side of Eq. (4) over an arbitrary region Ω. Eq. (5) is the equation of motion of the massless component $\mathbf{X}(q,r,s,t)$ of the immersed body. It simply says that the body $\mathbf{X}(q,r,s,t)$ moves at the local fluid velocity, i.e., by no-slip condition.

We remark that the previous versions of the pIB method in Refs. 4 and 5 also use Eqs. (1)-(5) as the basic framework. In fact, the pIB method was applied to simulate flows with a nonuniform density by using these equations only.[5] When the immersed boundary is elastic, we add the elastic force density generated from the deformation of the elastic body $\mathbf{X}(q,r,s,t)$ to the force term $\mathbf{F}(q,r,s,t)$ in Eq. (3).[4] Here we focus on an extension of the pIB method to the case in which the immersed boundary is a rigid body. Thus the pIB method is a unified framework for handling both elastic and rigid structures.

If the force density $\mathbf{F}$ in Eq. (3) were a function of the massless representative $\mathbf{X}(q,r,s,t)$ only, that is, if $\mathbf{Y}(q,r,s,t)$ were given, then Eqs. (1)-(5) would be complete and give the traditional IB formulation.[1–3] However, since the force density $\mathbf{F}$ is also a function of the unknown massive representative $\mathbf{Y}(q,r,s,t)$ of the rigid body, we need to take into account the rigid-body dynamics. To do that, let $\mathbf{Y}_{\rm cm}(t)$ be the center of mass of the body, and let $\{\mathbf{E}_1(t),\mathbf{E}_2(t),\mathbf{E}_3(t)\}$ be the orthonormal basis for a coordinate system fixed to the body with its origin at the center of mass. Then the position of the material points q, r, s of the body can be written as

$$\mathbf{Y}(q,r,s,t) = \mathbf{Y}_{\rm cm}(t) + c_1(q,r,s)\mathbf{E}_1(t) + c_2(q,r,s)\mathbf{E}_2(t) + c_3(q,r,s)\mathbf{E}_3(t). \tag{6}$$

Since the coordinates are fixed to the body, the coefficients $c_i(q,r,s)$'s are independent of time. Note that Eq. (6) allows for general curvilinear coordinates q, r, s that are fixed to the body. We get the special case of Cartesian coordinates by setting $c_1(q,r,s) = q$, $c_2(q,r,s) = r$, and $c_3(q,r,s) = s$.

Before proceeding further, let us introduce two notations: one is a 3×3 matrix $\mathcal{E}(t)$ of which the i-th column is the 3×1 vector $\mathbf{E}_i(t)$, and the second is the 3×1 vector-valued function $\mathbf{C}(q,r,s)$ of which the i-th component is $c_i(q,r,s)$. Then Eq. (6) is the same as

$$\mathbf{Y}(q,r,s,t) = \mathbf{Y}_{\rm cm}(t) + \mathcal{E}(t)\mathbf{C}(q,r,s). \tag{7}$$

Now the equations of motion of the rigid body $\mathbf{Y}(q,r,s,t)$ are a dynamical system for the variables $\mathbf{Y}_{\rm cm}(t)$, $\mathbf{E}_i(t)$, i = 1,2,3, $\mathbf{V}_{\rm cm}(t)$, and $\mathbf{L}(t)$, where $\mathbf{V}_{\rm cm}(t)$ is the velocity of the center of mass and $\mathbf{L}(t)$ is the angular momentum of the body. Each of these is a 3×1 vector, and its components are expressed in the laboratory frame of reference. The equations for $\mathbf{Y}_{\rm cm}(t)$ and $\mathbf{V}_{\rm cm}(t)$ are

$$\frac{d\mathbf{Y}_{\rm cm}}{dt} = \mathbf{V}_{\rm cm}(t), \tag{8}$$

$$M\frac{d\mathbf{V}_{\rm cm}}{dt} = -\int \mathbf{F}(q,r,s,t)dqdrds - Mg\,\mathbf{e}_3, \tag{9}$$

where $\mathbf{F}$ is defined in Eq. (3), $\mathbf{e}_3$ is a unit vector in the positive z direction, and g is the gravitational acceleration. Here and in the following, any integral with respect to q,r,s is understood to extend over the whole of the immersed body. In Equation (9), M is the excess mass of the body, i.e., the difference between its mass and the mass of the fluid displaced. Later on, we shall need the density of the excess mass, which we denote by $m(q,r,s)$. This is the difference between the density of the rigid body and the (constant) fluid density and, of course, $M = \int m(q,r,s)dqdrds$. Note that the motion of $\mathbf{Y}_{\rm cm}(t)$ depends on only the gravitational force and the total force generated by the stiff springs that connect the massive and massless descriptions of the immersed body. Thus the massive body $\mathbf{Y}(q,r,s,t)$ has no direct interaction with the surrounding fluid.

The equation for the angular momentum $\mathbf{L}(t)$ is

$$\frac{d\mathbf{L}}{dt} = \mathbf{T}(t), \tag{10}$$

where $\mathbf{T}$ is the total torque on the rigid body. In our case, the torque is the sum of the torques applied by all the springs that connect the points of the rigid body to their massless twins. It is important that the origin used in calculating this torque is the center of mass of the body. Thus the total torque is

$$\mathbf{T}(t) = \int (\mathbf{Y}(q,r,s,t) - \mathbf{Y}_{\rm cm}(t)) \times (-\mathbf{F}(q,r,s,t))dqdrds. \tag{11}$$

The equations for the orthonormal frame given by the $\mathbf{E}_i(t)$'s are

$$\frac{d\mathbf{E}_i}{dt} = \Omega(t)\times\mathbf{E}_i(t), \qquad i = 1,2,3, \tag{12}$$

where $\Omega(t)$ is the angular velocity of the body which can be calculated from $\mathbf{L}(t)$ as follows. First, recall the definition of the angular momentum $\mathbf{L}(t)$,

$$\begin{aligned}\mathbf{L}(t) &= \int (\mathbf{Y}(q,r,s,t) - \mathbf{Y}_{\rm cm}(t)) \times (m(q,r,s)\mathbf{V}(q,r,s,t))dqdrds \\ &= \int m(q,r,s)(\mathbf{Y}(q,r,s,t) - \mathbf{Y}_{\rm cm}(t)) \times (\mathbf{V}(q,r,s,t) - \mathbf{V}_{\rm cm}(t))dqdrds,\end{aligned} \tag{13}$$

where $\mathbf{V}(q,r,s,t)$ is the velocity of each point of the rigid body $\mathbf{Y}(q,r,s,t)$. In the second equation, we subtract $\mathbf{V}_{\rm cm}(t)$ from $\mathbf{V}(q,r,s,t)$ without any consequence because of the definition of center of mass.

Now, since the angular velocity $\Omega(t)$ is defined by

$$\mathbf{V}(q,r,s,t) - \mathbf{V}_{\rm cm}(t) = \Omega(t) \times (\mathbf{Y}(q,r,s,t) - \mathbf{Y}_{\rm cm}(t)), \tag{14}$$

by substituting this relation into (13) and using expression (7), we obtain

$$\mathbf{L}(t) = \int m(q,r,s)(\mathcal{E}(t)\mathbf{C}(q,r,s)) \times (\Omega(t) \times \mathcal{E}(t)\mathbf{C}(q,r,s))\, dqdrds. \tag{15}$$

This can be simplified with the help of the vector identity $\mathbf{u} \times (\mathbf{v} \times \mathbf{w}) = (\mathbf{u} \cdot \mathbf{w})\mathbf{v} - (\mathbf{u} \cdot \mathbf{v})\mathbf{w}$. In our case, since $\mathbf{u} = \mathbf{w}$, we have $\mathbf{u} \times (\mathbf{v} \times \mathbf{u}) = (|\mathbf{u}|^2 I_3 - \mathbf{u}\mathbf{u}^T)\mathbf{v}$, where $\mathbf{u}^T$ is the transpose of $\mathbf{u}$ and I_3 is the 3×3 identity matrix. Using the orthogonal property of the matrix $\mathcal{E}(t)$, we can therefore simplify (15) as follows:

$$\begin{aligned}
\mathbf{L}(t) &= \int m(q,r,s)((\mathcal{E}(t)\mathbf{C})^T(\mathcal{E}(t)\mathbf{C})I_3 - (\mathcal{E}(t)\mathbf{C})(\mathcal{E}(t)\mathbf{C})^T)\,\Omega(t)\, dqdrds \\
&= \int m(q,r,s)(\mathbf{C}^T\mathbf{C}I_3 - \mathcal{E}(t)\mathbf{C}\mathbf{C}^T\mathcal{E}(t)^T)\,\Omega(t)\, dqdrds \\
&= \mathcal{E}(t) \int m(q,r,s)(\mathbf{C}^T\mathbf{C}I_3 - \mathbf{C}\mathbf{C}^T)\, dqdrds\, \mathcal{E}(t)^T\,\Omega(t) \\
&= \mathcal{E}(t)\, I_0\, \mathcal{E}(t)^T\,\Omega(t),
\end{aligned} \tag{16}$$

where, for any matrix $\mathcal{A}$, $\mathcal{A}^T$ denotes the transpose of $\mathcal{A}$. The 3×3 matrix $\mathcal{E}(t)\, I_0\, \mathcal{E}(t)^T$ is the "moment of inertia tensor" which is expressed in terms of the time-independent matrix $I_0 = \int m(q,r,s)(\mathbf{C}^T\mathbf{C}I_3 - \mathbf{C}\mathbf{C}^T)\, dqdrds$ and the time-dependent orthogonal matrix $\mathcal{E}(t)$, i.e., the columns of which are the $\mathbf{E}_i(t)$'s. The angular velocity $\Omega(t)$ can be calculated by the inversion of Eq. (16), i.e., $\Omega(t) = \mathcal{E}(t)\, I_0^{-1}\, \mathcal{E}(t)^T\mathbf{L}(t)$.

The mathematical formulation of the pIB method for a three-dimensional viscous incompressible fluid interacting with a rigid body is fully described by Eqs. (1)-(5), (7)-(12), and (16). Consider the case in which $K \to \infty$ in Eq. (3). Then the massless body $\mathbf{X}(q,r,s,t)$ coincides with the massive body $\mathbf{Y}(q,r,s,t)$ and obeys rigid-body kinematics. Even though K cannot be infinite in practice, we can choose K to be so large that $\mathbf{Y}(q,r,s,t)$ and $\mathbf{X}(q,r,s,t)$ move as closely as we like. However, a large value of K may generate computational instability, and thus there is a trade-off between the size of K and the time step restriction. This issue will be discussed in Section IV A.

III. NUMERICAL IMPLEMENTATION OF THE pIB METHOD

For the numerical implementation to solve Eqs. (1)-(5), (7)-(12), and (16), we adopt a "formally" second-order IB method which was used in Refs. 24 and 25 and generalize it to consider the dynamics of the massive body that is connected to the massless body by stiff springs.[4,5] This method is based on the framework of a second-order Runge-Kutta method in which each time step is divided into two substeps: the preliminary and final substeps. The preliminary substep computes data at time level $n + \frac{1}{2}$ using data at time level n by a first-order accurate Euler method. Then the final substep uses the data at time levels n and $n + \frac{1}{2}$ to update the data at time level $n + 1$ by a second-order accurate midpoint rule.

Here we use a superscript to denote the time level. Let Δt be the time step, $\mathbf{X}^n(q,r,s)$ is shorthand for $\mathbf{X}(q,r,s,n\Delta t)$, and all other variables can be written in similar shorthands. A subscript is used to denote the spatial discretization of the immersed body. Thus $\mathbf{X}_k^n$, $k = 1,\ldots,N$, denote the marker points representing the immersed body where N is the total number of points used in the discretization.

Before describing the time iteration of the numerical scheme, we need the initialization of some variables. Initially the massive points $\mathbf{Y}_k^0$ are exactly the same as the immersed body points $\mathbf{X}_k^0$. Let us choose the initial orthonormal frame $\{\mathbf{E}_1^0, \mathbf{E}_2^0, \mathbf{E}_3^0\}$ for the coordinate system fixed at the body with

its origin at the center of mass as the standard basis for the 3D space $\{\mathbf{i},\mathbf{j},\mathbf{k}\}$. Then the corresponding orthonormal matrix $\mathcal{E}^0$ is the 3×3 identity matrix, and thus Eq. (7) determines the coordinates $\mathbf{C}_k$ for the point $\mathbf{Y}_k^0$ as

$$\mathbf{C}_k = \mathbf{Y}_k^0 - \mathbf{Y}_{\mathrm{cm}}^0, \tag{17}$$

where $\mathbf{Y}_{\mathrm{cm}}^0$ is the center of mass of the body at time 0. Note that $\mathbf{C}_k$'s are constants in time.

Let m_k be the excess mass density of the marker point $\mathbf{X}_k^0$ of the body. Then the total excess mass M of the body can be computed as

$$M = \sum_{k=1}^{N} m_k \Delta q \Delta r \Delta s, \tag{18}$$

where Δq, Δr, and Δs are the spatial meshwidths for the immersed body. Since the initial moment of inertia tensor I_0 used in (16) is independent of time, it is desirable to compute I_0 initially before the time iteration begins,

$$I_0 = \sum_{k=1}^{N} m_k (\mathbf{C}_k^T \mathbf{C}_k I_3 - \mathbf{C}_k \mathbf{C}_k^T) \Delta q \Delta r \Delta s. \tag{19}$$

Now a typical time iteration of the numerical scheme starts with the preliminary substep which proceeds from time level n to $n+\frac{1}{2}$ as follows.

First, we update the position of the massless body $\mathbf{X}_k^{n+\frac{1}{2}}$,

$$\mathbf{X}_k^{n+\frac{1}{2}} = \mathbf{X}_k^n + \frac{\Delta t}{2} \sum_{\mathbf{x}} \mathbf{u}^n(\mathbf{x}) \delta_h(\mathbf{x} - \mathbf{X}_k^n) h^3, \tag{20}$$

where $\mathbf{x} = (x_1, x_2, x_3)$ is the fluid mesh point and h is the spatial mesh width of the fluid domain. The function δ_h is a regularized version of the Dirac delta function.[1,3] Here and throughout the paper, $\sum_{\mathbf{x}}$ represents the sum over the cubic lattice in physical space on which the fluid variables are defined.

The key idea of extending the formally second-order method to the case for massive body is that the numerical treatments of the massive body and massless body are closely parallel to each other. Thus, we update the massive body $\mathbf{Y}_k^{n+\frac{1}{2}}$ in a similar manner to $\mathbf{X}^{n+\frac{1}{2}}$,

$$\mathbf{Y}_{\mathrm{cm}}^{n+\frac{1}{2}} = \mathbf{Y}_{\mathrm{cm}}^n + \frac{\Delta t}{2} \mathbf{V}_{\mathrm{cm}}^n, \tag{21}$$

$$\Omega^n = \mathcal{E}^n I_0^{-1} (\mathcal{E}^n)^T \mathbf{L}^n, \tag{22}$$

$$\mathbf{E}_i^{n+\frac{1}{2}} = \mathcal{R}\left(\frac{\Omega^n}{|\Omega^n|}, \frac{\Delta t}{2} |\Omega^n|\right) \mathbf{E}_i^n, \quad i = 1,2,3, \tag{23}$$

$$\mathbf{Y}_k^{n+\frac{1}{2}} = \mathbf{Y}_{\mathrm{cm}}^{n+\frac{1}{2}} + \mathcal{E}^{n+\frac{1}{2}} \mathbf{C}_k. \tag{24}$$

Here $\mathbf{V}_{\mathrm{cm}}^n$ is the velocity vector of the center of mass (a known value at time $n\Delta t$, like $\mathbf{u}^n$). The matrix $\mathcal{R}(\mathbf{v},\theta)$ in (23) represents the orthogonal matrix that describes the rotation through an angle θ about the axis specified by the unit vector $\mathbf{v}$. We can write $\mathcal{R}(\mathbf{v},\theta)$ explicitly as follows:

$$\mathcal{R}(\mathbf{v},\theta) = \cos\theta\, I_3 + (1-\cos\theta)\, \mathbf{v}\mathbf{v}^T + \sin\theta\, (\mathbf{v}\times). \tag{25}$$

Eq. (23) along with definition (25) is our discretization of Eq. (12). It guarantees that the $\mathbf{E}_i^{n+\frac{1}{2}}$'s remain exactly as mutually orthogonal unit vectors, which would not be the case if we used a typical Euler's method update.

Next, we calculate the two force densities $\mathbf{F}_k^{n+\frac{1}{2}}$ and $\mathbf{f}^{n+\frac{1}{2}}$,

$$\mathbf{F}_k^{n+\frac{1}{2}} = K(\mathbf{Y}_k^{n+\frac{1}{2}} - \mathbf{X}_k^{n+\frac{1}{2}}), \tag{26}$$

$$\mathbf{f}^{n+\frac{1}{2}}(\mathbf{x}) = \sum_k \mathbf{F}_k^{n+\frac{1}{2}} \delta_h(\mathbf{x} - \mathbf{X}_k^{n+\frac{1}{2}})\, \Delta q \Delta r \Delta s. \tag{27}$$

These are discretizations of Eqs. (3) and (4), respectively. The total torque can be computed in a similar fashion,

$$\mathbf{T}^{n+\frac{1}{2}} = \sum_{k=1}^{N} (\mathbf{Y}_k^{n+\frac{1}{2}} - \mathbf{Y}_{\mathrm{cm}}^{n+\frac{1}{2}}) \times (-\mathbf{F}_k^{n+\frac{1}{2}})\, \Delta q \Delta r \Delta s. \tag{28}$$

Once we obtain $\mathbf{f}^{n+\frac{1}{2}}$, we are ready to solve the Navier-Stokes equations,

$$\rho\Big(\frac{\mathbf{u}^{n+\frac{1}{2}} - \mathbf{u}^n}{\Delta t/2} + \frac{1}{2} \sum_{i=1,2,3} (u_i D_i^0 \mathbf{u} + D_i^0 (u_i \mathbf{u}))^n\Big) + \mathbf{D} p^{n+\frac{1}{2}} = \mu L \mathbf{u}^{n+\frac{1}{2}} + \mathbf{f}^{n+\frac{1}{2}}, \tag{29}$$

$$\mathbf{D} \cdot \mathbf{u}^{n+\frac{1}{2}} = 0, \tag{30}$$

where D_i^0 is the central difference formula for the partial derivative in the spatial direction denoted by i, where $i = 1,2,3$, and L is the standard 5-point discrete formula for Laplace operator. We use the skew-symmetric differencing for the convection term which enables us to convert correctly the force, torque, and power back and forth between Lagrangian and Eulerian forms by our scheme and to prove the conservation of energy for the spatially discretized IB method with uniform mass density.[1,24]

Again we have to calculate the velocity $\mathbf{V}_{\mathrm{cm}}^{n+\frac{1}{2}}$ and the angular momentum $\mathbf{L}^{n+\frac{1}{2}}$ in the same manner as $\mathbf{u}^{n+\frac{1}{2}}$,

$$\mathbf{V}_{\mathrm{cm}}^{n+\frac{1}{2}} = \mathbf{V}_{\mathrm{cm}}^n + \frac{\Delta t}{2M} \sum_{k=1}^{N} (-\mathbf{F}_k^{n+\frac{1}{2}})\, \Delta q \Delta r \Delta s - \frac{\Delta t}{2}\, g\, \mathbf{e}_3, \tag{31}$$

$$\mathbf{L}^{n+\frac{1}{2}} = \mathbf{L}^n + \frac{\Delta t}{2} \mathbf{T}^{n+\frac{1}{2}}. \tag{32}$$

This is simply a Euler's method for (9) and (10), respectively, and the preliminary substep completes.

The final substep uses data at time levels n and $n + \frac{1}{2}$ to update the corresponding data at time level $n + 1$ by the second-order accurate midpoint rule.

First, we update the massless body configuration $\mathbf{X}_k^{n+1}$ and massive body position $\mathbf{Y}_k^{n+1}$,

$$\mathbf{X}_k^{n+1} = \mathbf{X}_k^n + \Delta t \sum_{\mathbf{x}} \mathbf{u}^{n+\frac{1}{2}}(\mathbf{x}) \delta_h(\mathbf{x} - \mathbf{X}_k^{n+\frac{1}{2}}) h^3, \tag{33}$$

$$\mathbf{Y}_{\mathrm{cm}}^{n+1} = \mathbf{Y}_{\mathrm{cm}}^n + \Delta t \mathbf{V}_{\mathrm{cm}}^{n+\frac{1}{2}}, \tag{34}$$

$$\Omega^{n+\frac{1}{2}} = \mathcal{E}^{n+\frac{1}{2}}\, I_0^{-1}\, (\mathcal{E}^{n+\frac{1}{2}})^T\, \mathbf{L}^{n+\frac{1}{2}}, \tag{35}$$

$$\mathbf{E}_i^{n+1} = \mathcal{R}\Big(\frac{\Omega^{n+\frac{1}{2}}}{|\Omega^{n+\frac{1}{2}}|}, \Delta t |\Omega^{n+\frac{1}{2}}|\Big)\, \mathbf{E}_i^n, \quad i = 1,2,3, \tag{36}$$

$$\mathbf{Y}_k^{n+1} = \mathbf{Y}_{\mathrm{cm}}^{n+1} + \mathcal{E}^{n+1} \mathbf{C}_k. \tag{37}$$

Finally, we need to update the fluid velocity, the velocity of the center of mass, and the angular momentum of the immersed body,

$$\rho\Big(\frac{\mathbf{u}^{n+1} - \mathbf{u}^n}{\Delta t} + \frac{1}{2} \sum_{i=1,3} (u_i D_i^0 \mathbf{u} + D_i^0 (u_i \mathbf{u}))^{n+\frac{1}{2}}\Big) + \mathbf{D} p^{n+1} = \frac{1}{2} \mu (L\mathbf{u}^{n+1} + L\mathbf{u}^n) + \mathbf{f}^{n+\frac{1}{2}}, \tag{38}$$

$$\mathbf{D} \cdot \mathbf{u}^{n+1} = 0, \tag{39}$$

$$\mathbf{V}_{\mathrm{cm}}^{n+1} = \mathbf{V}_{\mathrm{cm}}^n + \frac{\Delta t}{M} \sum_{k=1}^{N} (-\mathbf{F}_k^{n+\frac{1}{2}}) \Delta q \Delta r \Delta s - \Delta t\, g\, \mathbf{e}_3, \tag{40}$$

$$\mathbf{L}^{n+1} = \mathbf{L}^n + \Delta t\, \mathbf{T}^{n+\frac{1}{2}}. \tag{41}$$

In order to solve the fluid equations ((29)-(30) and (38)-(39)), we use the assumption of periodic boundary conditions and adopt the discrete Fourier transform (implemented by the FFT algorithm). This is because the fluid equations can be solved efficiently by using the FFT algorithm. (Note, however, that there is no fundamental restriction on the fluid solver and the boundary conditions in the pIB method.) Though we use periodic boundary conditions in all three space directions for computational efficiency and also to avoid wall effects, we here "break" the periodicity in the vertical direction in the following way.

In all the problems considered, in order to keep a rigid body inside the computational domain, we generate an updraft within a rectangular slab that spans the bottom of the computational domain. To do that, we apply to the fluid equations a body force in the slab which is adjusted locally to achieve a desired velocity within the slab. The desired velocity, in turn, is adjusted by the following control mechanism:

$$\frac{dW_0(t)}{dt} = \gamma(z_{\text{target}} - Z_{\text{cm}}(t)) - \sigma W_{\text{cm}}(t), \tag{42}$$

where $Z_{\text{cm}}(t)$ and $W_{\text{cm}}(t)$ represent the z-components of the position and velocity of the center of mass of the massive body, respectively. These values can be computed in each time iteration. The velocity $(0,0,W_0(t))$ defines the desired updraft at time t, z_{target} is the fixed value representing the height which is targeted by the center of mass, and γ and σ are positive constants. The updraft increases or decreases depending on the height of the center of mass and also is damped according to $W_{\text{cm}}(t)$ in order to avoid large oscillations of the updraft velocity.

In addition to keeping the rigid body within the computational domain, the updraft flow within the bottom slab of the domain has the effect of preventing the features of the wake of the body from leaving the periodic domain at the top and from re-entering it at the bottom. Thus, the method to generate the updraft provides a nearly uniform upward flow from the bottom of the domain in which the rigid body falls.

IV. NUMERICAL VERIFICATION OF THE pIB METHOD

We verify the present pIB method by simulating some simple systems in which a fluid flows past rigid bodies in 2D and 3D. First, we simulate a flow past a cylinder in 2D and compare drag coefficients obtained by our numerical simulation with those found experimentally.[22] This has been widely used as a benchmark problem for numerical schemes.[24,26] We validate the present method further by a convergence study, which shows that it is first-order accurate. Although formally second-order accurate in space and time, the method of this paper is only first-order accurate spatially, since it is applied to problems whose solutions lack sufficient spatial smoothness for the formal second-order accuracy of the method to be realized in practice. Note that what we mean by a cylinder is an infinite circular cylinder which, when seen in a perpendicular plane to the cylinder, is a disc. Next, we consider two cylinders which simultaneously descend in a channel filled with a fluid. The simulation results will be compared with those in the literature. Finally, we simulate the sedimentation of a single sphere and the interaction of two descending spheres.[11] Throughout this section, we distribute the mass uniformly over the rigid body (cylinder or ball), and thus the center of mass is the geometrical center of the rigid body. Note, however, that mass could be distributed non-uniformly, which would affect the moment of inertia tensor.

In all the problems considered in this paper, we implement the pIB method (Eqs. (17)-(42)) described in Sec. III using Fortran 90 and use the HP workstation equipped with Intel(R) Xeon(R) 3.3 GHz CPU and 128 GB memory.

A. Flow past a single cylinder

When a fluid flows past a body which partially blocks the flow, the body feels a force in the flow direction which is called drag force. A drag force on a particular body can be characterized by

a dimensionless value, the drag coefficient C_D, which is computed by

$$C_D = \frac{F_D}{\frac{1}{2}\rho W_0^2 D}, \tag{43}$$

where ρ is the fluid density, W_0 is the far-field uniform velocity, and D is the reference length of the body which is the diameter of the cylinder in our case. The value F_D is the force exerted parallel to the flow direction. Here, F_D can be seen as the force per unit length of the infinite cylinder. See Ref. 22 for more details.

In typical computational simulations and physical experiments, the usual way to compute the drag coefficient of a body is to generate a uniform flow past the body which is fixed in the domain.[22,24,26] In our simulation, however, we want to test the apparatus of the pIB method, in particular the gravitational effect of mass, and so we drop the body and let it fall freely. In order to keep the body within the computational domain, we drive an upward flow from below at a velocity $W_0(t)$, and we adjust $W_0(t)$ by a control mechanism discussed in Sec. III, see Eq. (42). When the position of the body and the upward flow velocity $W_0(t)$ both settle down, the body feels no total force, and the drag force F_D of the body must be equal to its buoyant weight Mg, where M is the excess mass of the body and g is the gravitational acceleration. (In the present 2D problem, F_D is the drag force per unit length instead of the drag force, and M is the buoyant mass per unit length instead of the buoyant mass.) The value to which $W_0(t)$ settles down may be regarded as the uniform upward velocity that generates the drag force F_D.

Table I shows physical parameters of the problem. The fluid density is chosen as $\rho = 1.0$ g/cm^3 and the viscosity $\mu = 0.01$ g/(cm s). These values are the same as those of water. The computational domain is $[0, 1.2] \times [0, 2.4]$ cm^2, and the mesh width of the computational domain is uniform and fixed at $h = 1.2/512$ cm. The time step $\Delta t = 10^{-6}$ s, and the simulation requires 0.5×10^6 iterations (up to 0.5 s) which take about 10 h to complete. The left panel of Fig. 1 shows vorticity contours at $t = 0.5$ s for the freely falling cylinder in an upward flow in which we can observe oscillatory vortex shedding from the cylinder.

Unlike in a traditional IB calculation, the present pIB method uses the penalty parameter K which forces the two descriptions of the body to be close to each other. A large K causes a large force for any given displacement and may then lead to a computational instability which can be avoided by reducing the time step Δt. Our strategy of choosing the parameter K is by trial and error. We first choose an allowed distance between the two Lagrangian descriptions, then adjust K so that the computed distance between the two Lagrangian descriptions does not exceed the allowed distance and reduce the time step Δt, if needed to avoid numerical instability for a large K. Normally we choose the allowed distance to be one-tenth the meshwidth, i.e., $\|\mathbf{X} - \mathbf{Y}\|_\infty \le h/10$. This goal is achieved here by setting $K = 2.56 \times 10^{12}$ g/(cm^4 s^2). The upper right panel in Fig. 1 plots the maximum distance between the two descriptions $\mathbf{X}$ and $\mathbf{Y}$ of the cylindrical cross section. The plot shows that $\|\mathbf{X} - \mathbf{Y}\|_\infty$ is less than $h/10$.

In order to see that our control mechanism (42) has the desired effect that it makes the cylinder to stay at a constant height with a uniform inflow, we plot the applied upward velocity $W_0(t)$ (right-middle) and the height of center of mass of the cylinder $Z_{\text{cm}}(t)$ (lower right) as functions of time in Fig. 1. We can see that the height of the center of mass of the cylinder approaches a constant value, $z_{\text{target}} = 0.8$ cm, and that the speed of updraft $W_0(t)$, which the control mechanism requests to

TABLE I. Parameters of the simulation.

Parameter	Magnitude
Fluid density, ρ	1.0 g/cm^3
Fluid viscosity, μ	0.01 g/(cm s)
Cylinder diameter, D	0.1 cm
Cylinder excess mass per unit length, M	3.3×10^{-2} g/cm
Gravity, g	980 g cm/s^2
Domain size	1.2 cm $\times$ 2.4 cm

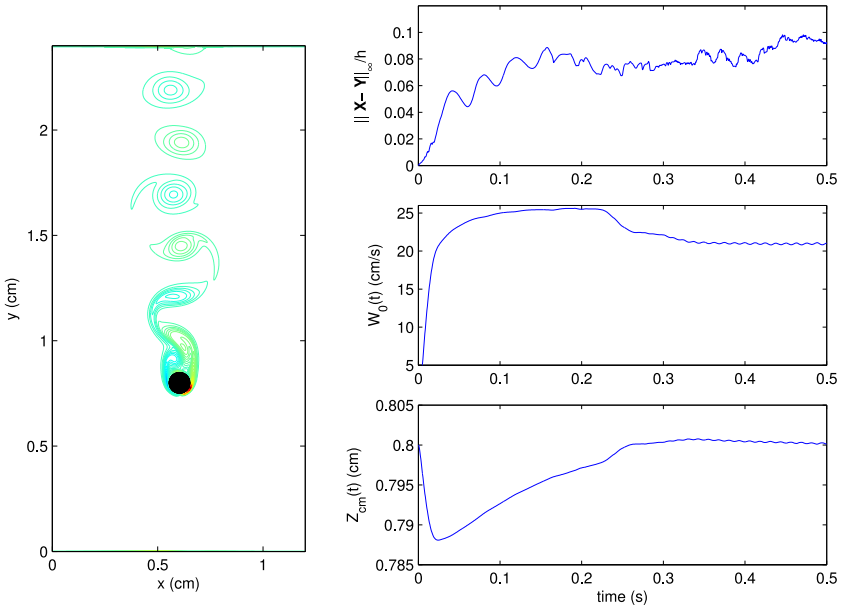

FIG. 1. The left panel shows the vorticity contours of flow past a freely falling cylinder at $t = 0.5$ s. Although falling freely through the water, the rigid body maintains a constant height because of the control mechanism that specifies the updraft velocity from below to levitate the body. The upper right panel plots the maximum distance between the two descriptions of the cross section of the cylinder. This plot shows that $\|\mathbf{X}-\mathbf{Y}\|_\infty$ is less than $h/10$. The right-middle panel represents the applied upward velocity $W_0(t)$ which, after about 0.4 s, stays around 21 cm/s. The lower right panel shows the height of the center of mass $Z_{\text{cm}}(t)$ which approaches a constant value, $z_{\text{target}} = 0.8$ cm.

support the falling body, approaches the constant value, $W_0(t) = 21$ cm/s. This is the exact goal that the control mechanism tries to achieve. Parameter values for control mechanism (42) are $\gamma = 10^4/\text{s}^2$ and $\sigma = 10^3/\text{s}$.

When the simulation approaches almost a steady state, the cylinder stays around one position with 0 velocity of the center of mass, in which case, using the almost uniform updraft $W_0(t)$, we can calculate two dimensionless quantities, the Reynolds number $\rho D W_0(t)/\mu$ and the drag coefficient $Mg/(0.5\,\rho\, W_0(t)^2\, D)$. Fig. 2 shows the Reynolds number (upper panel) and the drag coefficient (middle panel) as functions of time. Our simulation result gives a Reynolds number of about 210, in which case, the drag coefficient C_D of a cylinder is expected to be between 1.4 and 1.5 from the literature.[22,24,26] The drag coefficient C_D in our simulation is around 1.465, which is within the range in the literature. The lower panel plots the angular velocity ω_z of the cylinder which stays 0 initially for some time and then oscillates around 0. This oscillation of the angular velocity is a consequence of oscillatory vortex shedding.

We now perform a convergence study to verify that the rigid body dynamics in a fluid is correctly solved by the present pIB method. We consider the same problem as above, i.e., a freely falling cylinder in an upward flow. Then we vary the mesh sizes of the x and y directions of the domain as $(N_x, N_y) = (128, 256)$, $(256, 512)$, $(512, 1024)$, and $(1024, 2048)$ so that the mesh width becomes $h = 1.2/N_x$ correspondingly. We also choose Δs and Δt proportional to h, so that the refinements for the fluid mesh width, the boundary mesh width, and the time step duration are done by the same factor. When we refine the mesh width and time step, we increase the penalty parameter as $K = 9.7656 \times 10^6 N_x^2\ \text{dynes/cm}^5$.

Table II shows the Reynolds numbers and drag coefficients, respectively, for each case of the four mesh sizes ($N_x = 128$, 256, 512, and 1024). These dimensionless quantities are averaged temporally from $t = 0.4$ to $t = 0.5$ in the almost steady state. We can see that, when N_x increases, the Reynolds number increases and drag coefficient decreases. However, the increment in Reynolds number and the decrement in drag coefficient reduce as N_x increases, and the difference of the two dimensionless quantities between the cases of two consecutive grid sizes decreases, which suggests

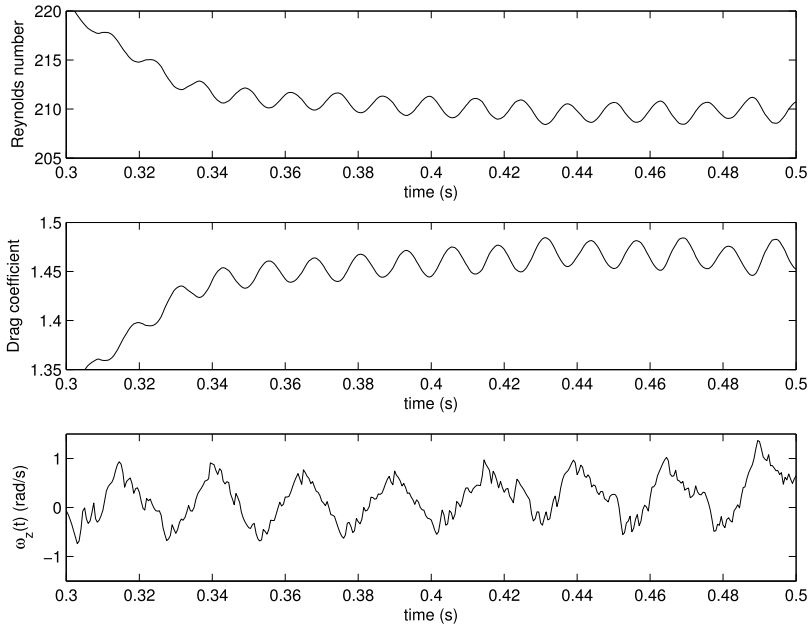

FIG. 2. The Reynolds number (upper), the drag coefficient (middle), and the angular velocity ω_z (lower) as functions of time for 2D cylinder.

convergence. Note that the drag coefficients are between 1.4 and 1.5 only when $N_x = 512$ and 1024, i.e., when the computational grids are fine enough.

Table III shows the convergence ratios of the Reynolds number, drag coefficient, and velocity field. The convergence ratio of the velocity field is computed by $(\|u_{N_x} - u_{2N_x}\|_2^2 + \|v_{N_x} - v_{2N_x}\|_2^2)^{1/2}/(\|u_{2N_x} - u_{4N_x}\|_2^2 + \|v_{2N_x} - v_{4N_x}\|_2^2)^{1/2}$ for each of the cases $N_x = 128$ and 256. The convergence ratios of Reynolds number and drag coefficient are defined similarly. Whereas the updraft $W_0(t)$ used in computing the Reynolds numbers and drag coefficients is the averaged value from $t = 0.4$ s to $t = 0.5$ s, the velocity field is chosen at $t = 0.1$ s. One can see that the convergence ratios for the velocity field are around two, which indicates the first-order accuracy of the present method. As remarked above, the IB method is typically first-order accurate, despite its formal second-order accuracy. There are some special situations in which actual second-order accuracy is achieved,[4] but these seem to be those that avoid a delta-function layer of force at the solid-fluid interface. Such a delta-function layer is needed here, despite the thickness of the solid, to enforce the no-slip condition at a rigid boundary.

B. Two freely falling cylinders

Here, we consider the interaction between two circular cylinders falling freely in a steady fluid. We choose a computational domain $[0,2] \times [0,8]$ cm^2 filled with a fluid of which the viscosity is 0.01 g/(cm s) and the density is 1 g/cm^3. The excess mass densities of the two cylinders are 0.01 g/cm^3 and their radii are both 0.1 cm. Gravity with $g = 980$ cm/s^2 acts in the negative y-direction. The simulation is started at $t = 0$ s by releasing the two cylinders at the initial positions (1.0 cm, 7.2 cm) and (1.0 cm, 6.8 cm). The meshwidth is $h = 2/256$ cm, the time step is

TABLE II. Reynolds numbers and drag coefficients for meshsize N_x.

N_x	128	256	512	1024
Reynolds number	188	203	210	213
Drag coefficient	1.82	1.56	1.46	1.42

TABLE III. Convergence ratios.

	$N_x = 128, 256, 512$	$N_x = 256, 512, 1024$
Reynolds number	2.30	1.84
Drag coefficient	2.6	2.0
Velocity field	1.66	1.90

$\Delta t = 5 \times 10^{-5}$ s, and the final time is 5 s which requires about 10 h to complete the simulation. This case is identical to the one presented in Ref. 14 except that we here use periodic boundary conditions for the fluid equations instead of Dirichlet boundary conditions used in Ref. 14.

The left panel of Fig. 3 shows the motion of the falling cylinders at some chosen times, and the right panels plot the streamlines at those times. It is known that two cylinders dropped close to each other in a Newtonian fluid undergo drafting, kissing, and tumbling.[19,16,27] Initially the two cylinders have the same downward acceleration. Later, the velocity of the upper cylinder becomes faster than that of the lower one, since the lower cylinder is falling into essentially still fluid, but the upper cylinder is falling through fluid that is being pulled downward by the lower cylinder. Thus the lower cylinder drafts the upper one continuously (t = 1.0 s), and then the two cylinders kiss and temporarily move together like one rigid body (t = 2.0 s). Then an instability sets in, and the upper cylinder tumbles over the lower one (t = 3.0 s). After tumbling through an angle of about 130° is complete, the cylinders come apart and continue to fall (t = 3.5 s). Note that, as a result of symmetry breaking, the cylinders have both been displaced horizontally in the same direction and by different amounts, so that they are no longer aligned one below the other.

Fig. 4 shows the centers of mass $(X_{\text{cm}}(t), Y_{\text{cm}}(t))$ of the two cylinders (upper panels), their falling speeds $V_{\text{cm}}(t)$ (lower-left), and their angular velocities ω_z of rotation about their centers of mass (lower-right) as functions of time. The vertical velocity of the initially upper cylinder is larger in magnitude than that of the lower cylinder until t = 1.2 s, and then both vertical velocities are the

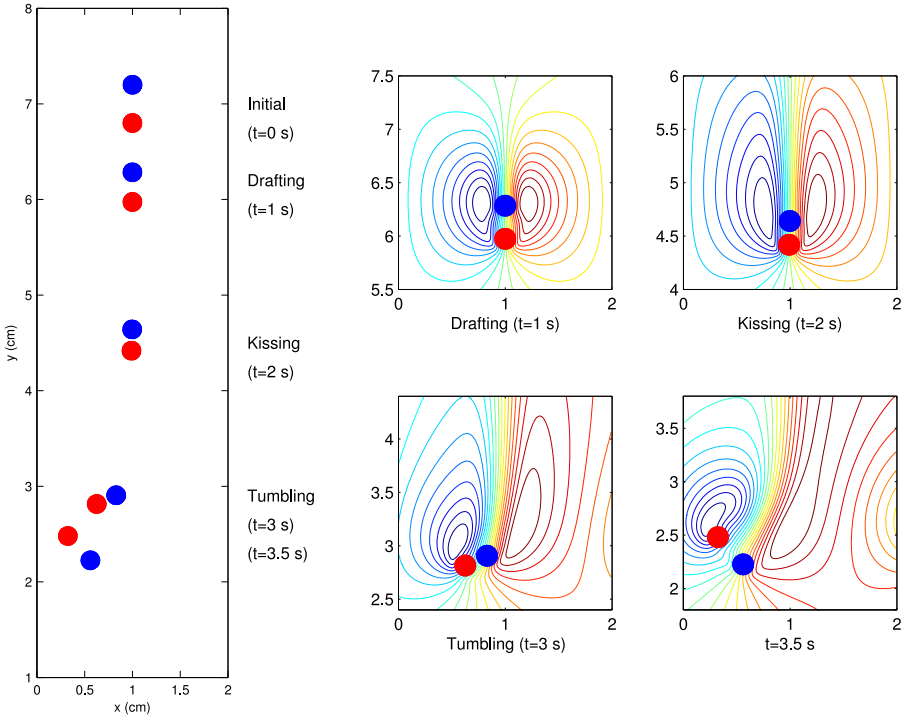

FIG. 3. Numerical simulation of drafting, kissing, and tumbling of two cylinders falling in fluid. The left panel shows the cylinder positions at some selected times, and the right panels plot the streamlines at those selected times. Throughout the figure, blue color indicates the cylinder that is initially the upper one, and red indicates the initially lower cylinder.

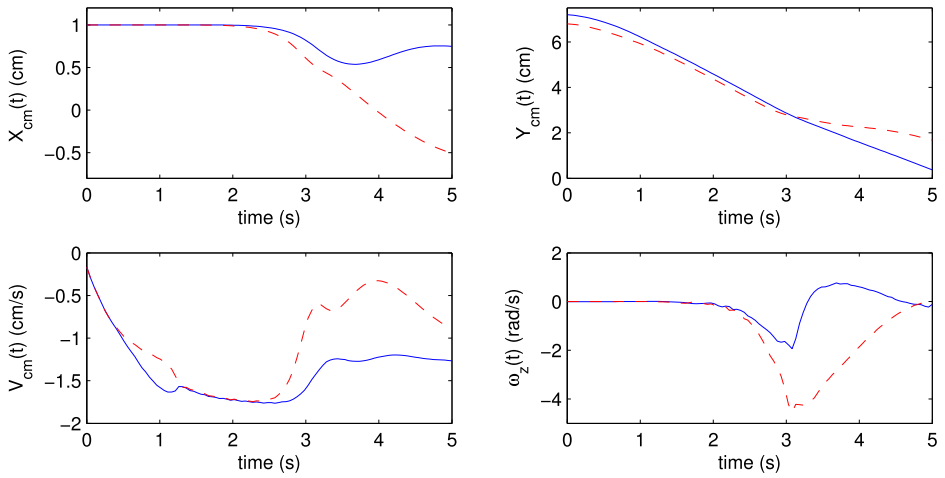

FIG. 4. The horizontal and vertical positions of the centers of mass (upper panels), the vertical velocities of the centers of mass (lower-left), and the angular velocities of rotation of the two cylinders about their centers of mass (lower-right). In the plots, the solid blue lines refer to the initially upper cylinder, and the dashed red lines refer to the initially lower one.

same from $t = 1.2$ s to 2.6 s. These correspond to drafting and kissing, respectively. After about $t = 2.5$ s, the vertical velocities, the x-components of the center of mass of the two cylinders, and the angular velocities of rotation of the two cylinders bifurcate and the differences of these values become larger for some time. These correspond to the tumbling followed by separation. Our numerical results in Figures 3 and 4 have a good agreement with data in Refs. 14, 19, and 16.

C. Sedimentation of spherical balls

In this section, we consider the descent under gravity of a spherical ball through a fluid and the interaction of two such descending spherical balls. These are the 3D analogs of the 2D problems considered in Sec. IV B. In the first case, we drop a ball with radius 0.05 cm in the domain $[0,1.2] \times [0,1.2] \times [0,2.4]$ cm^3, and we drive an upward flow from below at a velocity $W_0(t)$ determined by control mechanism (42). The ball has excess mass density 2 g/cm^3 and total excess mass $M = 1.05 \times 10^{-3}$ g. The other physical parameters are the same as those in Table I. The mesh width of the computational domain is fixed at $h = 1.2/128$ cm, and the time step duration $\Delta t = 5 \times 10^{-6}$ s. The total iteration number 4×10^5 (up to 2 s) requires about 126 h to complete the simulation.

The left panel of Fig. 5 shows the streamlines of the flow past a freely falling ball in an upward flow in which we can observe the vortex shedding above the ball. The right panels of Fig. 5 show the Reynolds number (upper) and the drag coefficient (lower) as functions of time after the height of the center of mass of the ball approaches a constant value, $z_{\text{target}} = 0.8$ cm, with an almost uniform speed of updraft $W_0(t) \approx 13$ cm/s. The Reynolds number is around 130 (dotted line), in which case, the drag coefficient C_D of a 3D ball is expected to be around 0.92 based on experimental data.[22] We can see, however, that our result is around 1.5 (dotted line) which is larger than the experimental data, see the dotted line in the lower-right panel.

The difference between our result and the real data comes from a numerical effect that is inherent in the IB method: since the numerical implementation of the IB method uses a continuous delta function with a finite support, the effect of the immersed body extends slightly beyond the real body. When we use the four-point supported delta function,[1,3] it has been documented in Ref. 28 that immersed boundaries may have an effective thickness of as much as $2 \times 1.42\,h$ where h is the meshwidth of the computational domain. This would increase the radius of the ball by $1.42\,h$ and its diameter by $2 \times 1.42\,h$. The solid line in the right panels of Figure 5 represents the Reynolds number and the drag coefficient of the ball with the effective radius 0.05 cm + $1.42\,h$. Calculating the drag coefficient in this way, we get $C_D = 0.93$, which is close to the experimental data $C_D = 0.83$ given in Ref. 22 when the Reynolds number is 165.

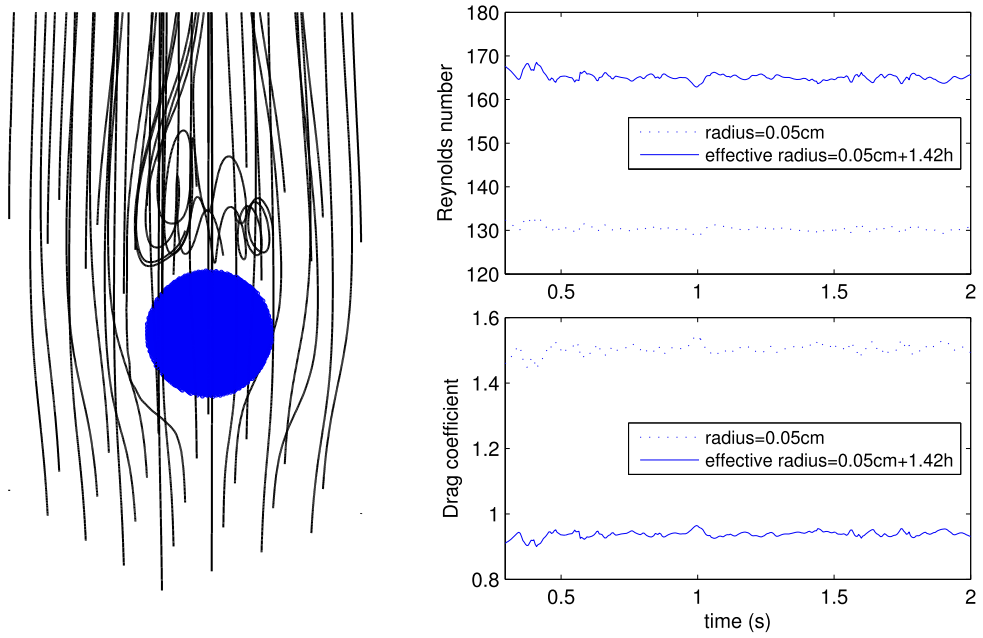

FIG. 5. The left panel shows the streamlines of flow past a freely falling ball at $t = 2$ s. The right panels depict the Reynolds number (upper) and the drag coefficient (lower) as functions of time for the 3D ball.

As in the case of two falling cylinders in fluid, it is known that two balls which are initially aligned vertically fall with the behaviors called "drafting, kissing, and tumbling."[11] The upper panels of Fig. 6 show the interaction of two descending balls together with streamlines of the flow at some chosen times: $t = 0.05$ s, 0.2 s, 0.25 s, and 0.35 s. The wake behind the lower ball reduces the drag on the trailing ball which thus falls faster than the leading ball. This is called drafting ($t = 0.05$ s), and the increasing falling speed draws the trailing ball into a kissing contact with the leading ball ($t = 0.2$ s). Since an elongated rigid body is unstable when its center line is along the flow direction, the kissing balls, which temporarily act somewhat like such a rigid body (but see below), tend to tumble ($t = 0.25$ s). After tumbling, the balls move apart and continue to fall with almost no interaction ($t = 0.35$ s). This well-known mechanism of the interaction of two descending balls is clearly seen in Fig. 6, in which we have used two identical balls with the same properties as the above single descending ball. The initial positions of the two balls were vertically aligned with their centers separated by 0.3 cm, which is 6× the radius of either ball.

The middle panel of Fig. 6 depicts the distance between the centers of the two balls as a function of time, which also shows the behaviors of drafting, kissing, tumbling, and falling separately. The lower panel shows the x-component $\omega_x(t)$ (solid line with "∘") and z-components $\omega_z(t)$ (solid line) of the angular velocity of the two balls as functions of time. The blue color refers to the ball that is initially the upper one, and the red refers to the initially lower ball. The y-component of the angular velocity behaves similarly to the x-component. Both the x and z components of the angular velocities of the two balls are 0 until around 0.18 s when the kissing balls start to rotate. In this tumbling motion, the z component of the angular velocity of the two balls is smaller than the x component. Also the initially lower ball (red) has a larger angular velocity than the initially upper ball (blue). This indicates that, in the kissing state, the two balls are *not* rotating as a rigid body. (If they were, their angular velocities would be the same.) Instead, the initially lower ball is rotating and the initially upper ball is more or less in a state of orbital translation around it, without much rotation.

V. AUTOROTATION OF A MAPLE SEED

In this section, we introduce a model of a single maple seed and simulate the flight dynamics as it descends. Many samaras or winged seeds such as maple seeds exhibit autorotational flight

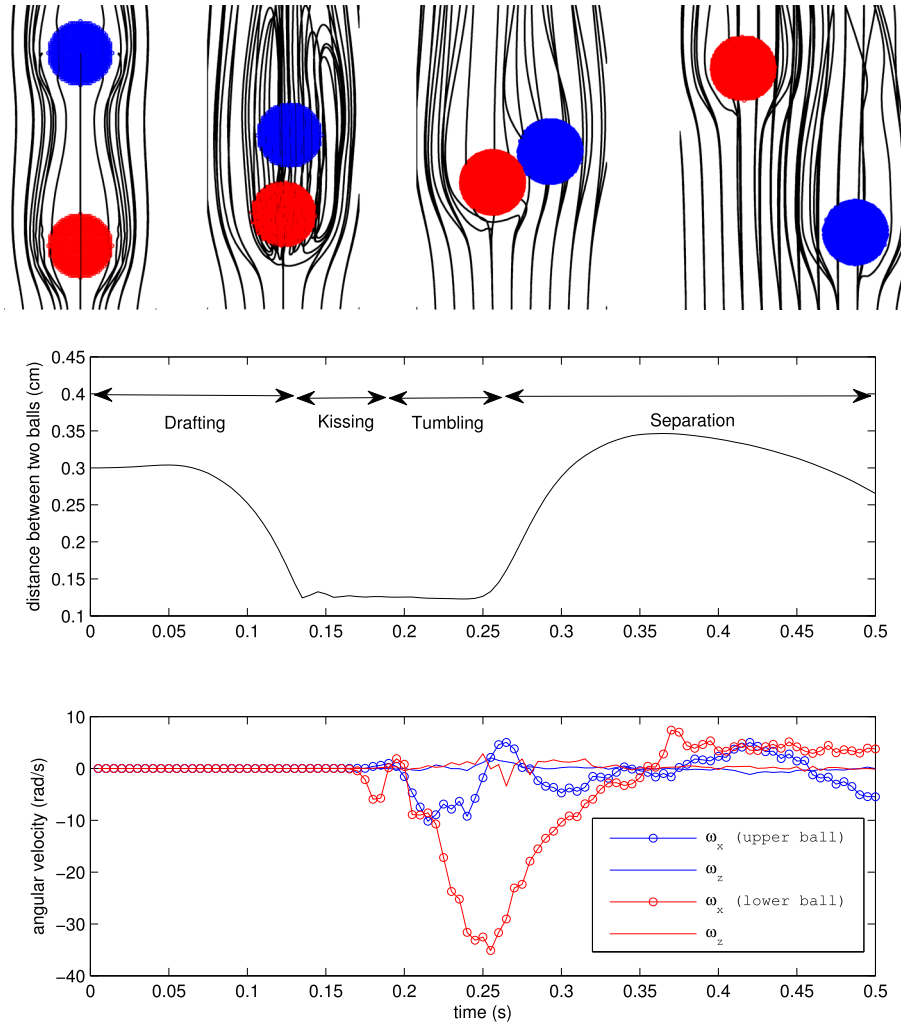

FIG. 6. The upper panels show the interactive motion of a pair of balls settling in a Newtonian fluid with streamlines: from right to left, drafting at $t = 0.05$ s, kissing at $t = 0.2$ s, tumbling at $t = 0.25$ s, and falling separately at $t = 0.35$ s. The middle panel depicts the distance between the centers of the two balls, and the lower panel shows the x-component $\omega_x(t)$ (solid line with "$\circ$") and the z-component $\omega_z(t)$ (solid line) of the angular velocities of the two balls. The blue color refers to the ball that is initially the upper one, and the red refers to the initially lower ball.

during their fall. Autorotation of winged maple seeds, which is the result of a delicate equilibrium between gravity, inertia, and aerodynamic forces, reduces the falling speed and increases the flight time and thus the distance which maple seeds can reach. Many experimental and theoretical studies have been done to describe and explain the flight performance of maple seeds[18,29,23,30–32] and to determine how the rate of descent, the spinning rate of autorotation, and the coning angle of the rotating seeds depend on the geometrical configuration, total mass, and distribution of mass within a maple seed.

Our model of maple seed has two parts: one is the "nut" which we model as a spherical ball and the other is the "seed wing" which has the shape of a leaf appended to the nut, see Fig. 7 which shows a picture of a real maple seed (left) and our model of the maple seed as seen in the xy-plane, which contains the seed wing (right). The configuration of the model seed wing is planar. In body coordinates, it is the part of the xy-plane that is enclosed between two parabolas,

$$4h_1x(x-L)/L^2 \le y \le -4h_2x(x-L)/L^2, \quad 0 \le x \le L, \tag{44}$$

where L is the length and $h_1 + h_2$ is the maximal width of the seed wing.

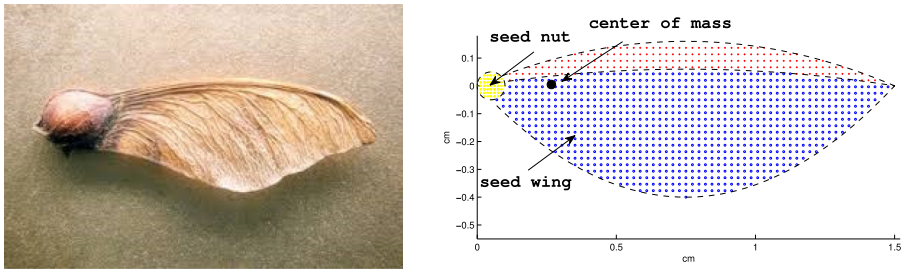

FIG. 7. A real maple seed (left) and the reference configuration of the model of a maple seed indicating its center of mass (right). The grid points on the seed wing represent the marker points of the immersed body. The mass densities of the upper part (red markers) and lower part (blue markers) of the seed wing are 0.028 g/cm^2 and 0.0028 g/cm^2, respectively. The position of the center of mass (black marker) is $\mathbf{Y}_{\text{cm}}(0) = (0.267, 0.005, 0)$ cm^3.

The dynamics of a maple seed depends on its geometrical shape, its total mass, and the location of its center of mass. The nut in our model is a ball with radius 0.05 cm and mass density 18.0 g/cm^3. The parameters which define the seed wing are chosen as $h_1 = 0.4$ cm, $h_2 = 0.16$ cm, and $L = 1.5$ cm, which make the seed wing area be $\frac{2}{3}(h_1 + h_2)L = 0.56$ cm^2. The seed wing is divided into two parts by a parabola $y = -4h\,x(x - L)/L^2$, where $h = 0.06$, see the blue and red markers in Fig. 7. The mass densities of the upper part (red markers) and lower part (blue markers) of the seed wing are 0.028 g/cm^2 and 0.0028 g/cm^2, respectively. These two different mass densities of the seed wing shift the center of mass to the upper part of the wing which then becomes the leading edge when the maple seed rotates. With these values of the parameters, our model of the maple seed has the total mass $M = 0.013$ g and the position of the center of mass in the reference configuration $\mathbf{Y}_{\text{cm}}(0) = (0.267, 0.005, 0)$ cm^3. The wing area and the total mass of our model are equal to the values given in Refs. 18 and 23. The fluid density and viscosity are the same as those of air: $\rho = 0.0012$ g/cm^3 and $\mu = 0.0002$ g/(cm s). The computational domain is $[0, 10] \times [0, 10] \times [0, 20]$ cm^3, and the mesh width of the computational domain is $h = 10/128$ cm, which is uniform and fixed in time. We use the time step duration $\Delta t = 5 \times 10^{-6}$ s and the final time $t = 1$ s which require about 70 h to complete the simulations.

As in the simulations of Sec. IV, while the maple seed is falling, we drive an updraft from below to keep the seed within the computational domain. Here, however, we do not use a control mechanism but instead prescribe a constant updraft velocity $W_0(t) = 100$ cm/s for all time t. Also the initial fluid velocity is $\mathbf{u} = (0, 0, 100$ cm/s) and the initial velocity of the center of mass is $\mathbf{V}_{\text{cm}} = (0, 0, 100$ cm/s). This makes the descent velocity, which is defined as $W_{\text{cm}}(t) - W_0(t)$, be the same as if the seed had been dropped from rest in still air and turns out to keep the seed within the computational domain.

Figs. 8(a) and 8(b) show the typical motion of the falling maple seed. The two pictures (a) and (b) have different initial orientations of the maple seed as shown at the top of each panel. We can observe that, independent of the initial orientation, the seed nut initially falls faster than the seed wing. This is because the drag force of the surrounding fluid is higher on the seed wing than on the nut. After a transitional phase, the maple seed in both cases settles down to a steady spinning motion with the upper and heavier part of the seed wing being the leading edge of the rotation.

Figs. 8(c) and 8(d) show the streamlines around the falling maple seed in the steady rotational state. The maple seeds in (c) and (d) are viewed from the more massive part of the seed wing (red markers in Fig. 7) and from the nut, respectively. We can observe that the upward uniform flow below the maple seed veers away from the maple seed. We can also see from (d) that the streamlines are more accumulated in the region around the heavier part of the seed wing (red markers), which implies that the flow moves faster around the heavier part. This means that the pressure is smaller around the heavier part of the seed wing which then becomes the leading edge of the rotational motion of the maple seed.

Autorotational motion of a maple seed can be characterized by the descent rate, the speed of rotation, and the coning angle.[23,18,29–32] These physical quantities, which are determined by the balance between the lift force due to the spinning motion of the maple seed and the gravitational

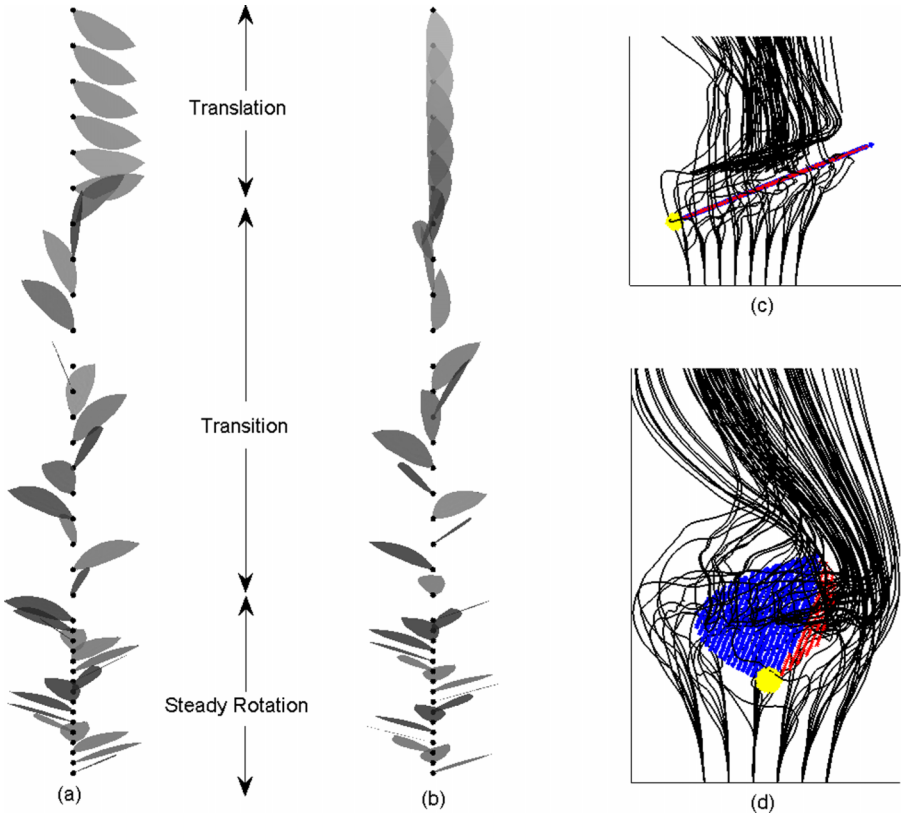

FIG. 8. Motion of a maple seed dropped from two different initial orientations in a constant-velocity updraft. In (a) and (b), three phases of motion can be discerned. First, the maple seed falls without much change in orientation (the frames labeled "translation" in the figure). Then the nut starts to lead as air resistance takes hold of the wing, and the seed starts to rotate ("transition"). The transition phase involves only a little more than one cycle of rotation, and after that the wing becomes more nearly horizontal, the speed of descent slows, and the motion becomes steady ("steady rotation"). Panels (c) and (d) show streamlines during the steady rotation phase. In (c), the wing is viewed with the leading edge in front, and in (d) it is viewed with the nut facing forward. Note that the leading edge is on the part of the wing with the higher mass density, which is colored red in the figure.

force, can be easily computed in our computational procedure. Since we drive an upward flow from below at a velocity $W_0(t)$, the descent velocity (a negative quantity) is the updraft velocity $W_0(t)$ subtracted from the z-component $W_{\mathrm{cm}}(t)$ of the velocity of the center of mass, i.e., $W_{\mathrm{cm}}(t) - W_0(t)$. The upper-left panel of Fig. 9 depicts the descent velocity as a function of time. It shows that the descent velocity of the maple seed increases rapidly in magnitude at the beginning of the fall, then goes through a transitional phase, and finally settles down to about −87 cm/s, which is similar to the descent velocity observed in Refs. 23, 18, and 32.

The upper-right panel of Fig. 9 shows the angular momentum of the falling maple seed as a function of time. The angular momentum is initially 0, and then the seed begins to accelerate downward with a rotary spinning motion being initiated. The x component L_x of the angular momentum changes irregularly at first and then settles down to a repetitive oscillation. The y component L_y, which is not shown in the figure, behaves similarly. The z component L_z of the angular momentum is initially 0, and, after a transient that lasts about 0.6 s, settles down to a constant value. This constant value of L_z indicates that the maple seed flies in the air with screw-like rotation during its fall. If we project the image of the maple seed to the xy-plane and watch it from above or below, we can see a spinning motion, but there is no other viewpoint from which the motion looks so simple.

Maple seeds start to rotate soon after their release. Rotation reduces the descent rate and increases the distance that wind can carry the seeds. When a maple seed rotates in a steady state, the angle between the maple seed and the xy plane becomes almost a constant. This angle is called the

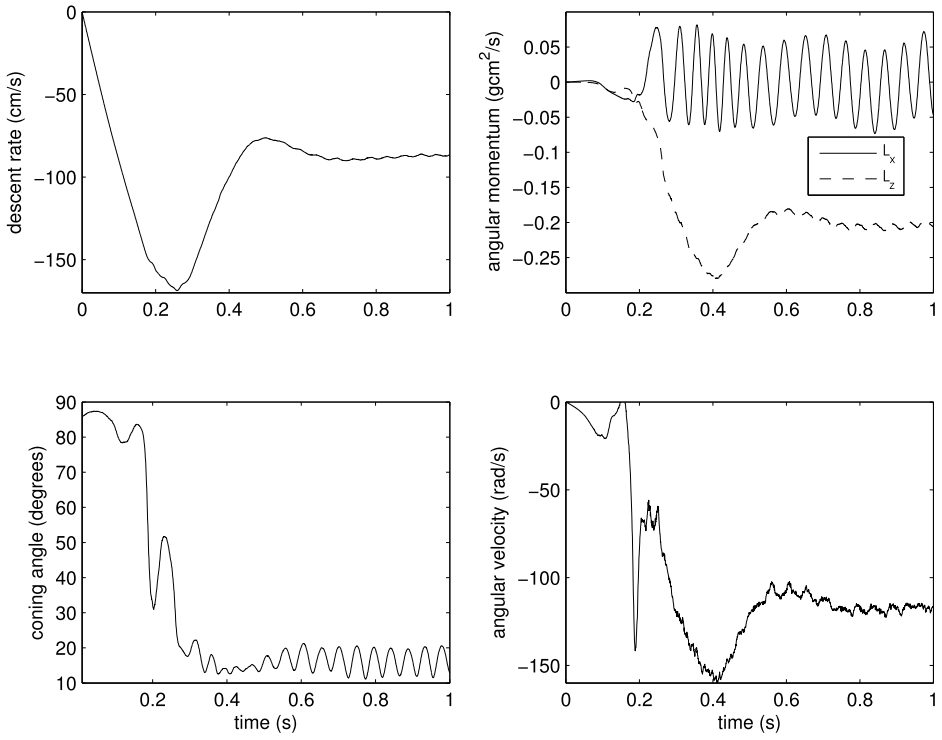

FIG. 9. The descent velocity (upper-left), the x and z components L_x and L_z of the angular momentum (upper-right), the coning angle (lower-left), and the azimuthal angular velocity ω_z (lower-right) of a falling maple seed. After a transient period, the descent velocity stays around −87 cm/s, the x component L_x of the angular momentum settles down to a repetitive oscillation, and both the z component L_z of the angular momentum and the azimuthal angular velocity ω_z become approximately constant. Thus the maple seed falls and rotates at almost constant linear and azimuthal angular velocities. In this steady rotational state, the coning angle is around 16.34° and the azimuthal rotational frequency $\omega_z/2\pi$ is 18.635 Hz.

coning angle which can be computed by

$$\beta = \arctan \frac{\sqrt{L_x^2 + L_y^2}}{|L_z|}, \tag{45}$$

where $\mathbf{L} = (L_x, L_y, L_z)$ is the angular momentum. The lower-left panel of Fig. 9 depicts the coning angle of the falling maple seed as a function of time. We can observe that, after a transient, the maple seed starts to rotate and maintains a fairly constant coning angle. The transient time is around 0.6 s, after which the coning angle stays around 16.34° which is comparable to the coning angle 15.0° in Ref. 23 and 17.1° in Ref. 32.

The lower-right panel of Fig. 9 shows the z component of the angular velocity of the maple seed as a function of time. The z component of the angular velocity, which describes azimuthal rotation, starts at 0, varies irregularly for about 0.7 s, and then settles down to about −117 rad/s. This indicates that, after a transient, the maple seed settles down to a steady spinning motion at an almost constant spinning rate with one direction of the rotation. The leading edge of the rotation turns out to be the heavier part of the seed wing. When the maple seed is in the steady rotational state, the azimuthal rotational frequency $\omega_z/2\pi$ is about 18.635 Hz or approximately 1118 rotations per minute (rpm). This value is lower than the rotational speed 1800 rpm in Ref. 23 and 1652 rpm in Ref. 32 but is 3 times higher than the value given in Ref. 18.

We conclude this section with some remarks on Zhao's model for a maple seed in Ref. 18. Zhao used the original version of the pIB method[4] by considering the maple seed as an elastic body with stretching and bending resistances. As the coefficients of these stretching and bending energy functionals get larger, the maple seed becomes less flexible (or more rigid). Even though we assume in this study that the maple seed is perfectly rigid, we can combine Zhao's method and the present

pIB method to model a maple seed with both flexible and rigid parts. The investigation of the flight performance of the combined flexible/rigid maple seed will be a possible future work. Zhao's and our models are almost identical in terms of the shape, mass, and area of the maple seed; however, the simulation results on the descent velocity, angular velocity, and coning angle are quite different. (The results of our model are closer to the experimental data in Ref. 23.) The difference between these two simulation results might come from different rigidity, grid resolution, and mass density distribution.

VI. SUMMARY AND CONCLUSIONS

We have introduced a new extension of the pIB method that can handle a rigid body immersed in a viscous, incompressible fluid. This method conceptually separates the rigid body into two parts, one of which has the mass density of the ambient fluid, while the other one carries the excess mass of the body. The part with the mass density of the ambient fluid is modeled as a part of the fluid, and the other part is modeled as a rigid body. The two parts are linked by a system of stiff springs, which effectively force their motions to agree.

This approach has the virtue of simplicity. The fluid equations are defined on the whole domain, including the region occupied by the body, and they have constant density and viscosity everywhere. (The viscosity within the region occupied by the body has no physical consequences, since the motion there is effectively a rigid-body motion anyway.) Also, the rigid-body equations are those of Euler, with forces and torques applied by the stiff springs that link the body to the fluid. Because the springs are not infinitely stiff, we avoid the complication of imposing a rigid body constraint on the fluid motion. The method is easy to implement as an add-on to any incompressible Navier-Stokes solver for the uniform density, uniform viscosity case.

We have applied this new extension to some benchmark problems, including sedimentation in 2D and 3D, as well as the autorotation of a falling maple seed. Since our aim here was only to illustrate the new method, we have not pursued these applications in as much detail as they deserve. In particular, the maple seed problem should be studied further to delineate how the shape of the seed and its mass distribution influence its autorotation and ultimately its descent speed. Such studies would benefit, no doubt, from adaptive mesh refinement.[33] There is quite a variety of shapes and sizes of maple seeds in nature, and it would be interesting to know whether each of them is somehow optimally adapted to a particular set of environmental conditions.

More generally, it is our hope that this new method will find many applications to the fluid dynamics of rigid immersed bodies, possibly of complicated geometry, either by themselves or in combination with the kinds of elastic immersed boundaries that have always been the application domain of the immersed boundary method.

ACKNOWLEDGMENTS

The first author was supported by the National Research Foundation of Korea grant funded by the Korean Government (No. 2015R1A2A2A01005420). The second author was supported in part by the National Science Foundation (USA) under Grant No. OCI 1047734.

[1] C. S. Peskin, "The immersed boundary method," Acta Numer. **11**, 479-517 (2002).
[2] C. S. Peskin, "Numerical analysis of blood flow in the heart," J. Comput. Phys. **25**, 220-252 (1977).
[3] C. S. Peskin and D. M. McQueen, "Fluid dynamics of the heart and its valves," in *Case Studies in Mathematical Modeling: Ecology, Physiology, and Cell Biology* (Prentice Hall, Englewood Cliffs, NJ, 1996), pp. 309-337.
[4] Y. Kim and C. S. Peskin, "Penalty immersed boundary method with an elastic boundary with mass," Phys. Fluids **19**(5), 053103 (2007).
[5] Y. Kim and C. S. Peskin, "Numerical study of incompressible fluid dynamics with nonuniform density by the immersed boundary method," Phys. Fluids **20**, 062101 (2008).
[6] J. J. Heys, B. Knott, T. Gedeon, and Y. Kim, "Modeling arthropod filiform hair motion using the penalty immersed boundary method," J. Biomech. Eng. **41**(5), 977-984 (2008).
[7] C. Duncan, G. Zhai, and R. Scherer, "Modeling coupled aerodynamics and vocal fold dynamics using immersed boundary methods," J. Acoust. Soc. Am. **120**, 2859-2871 (2006).
[8] Z. Feng and E. E. Michaelides, "The immersed boundary-lattice Boltzmann method for solving fluid-particles interaction problems," J. Comput. Phys. **195**, 602-628 (2004).

[9] M. Garcia, J. Gutierrez, and N. Rueda, "Fluid-structure coupling using lattice-Boltzmann and fixed-grid FEM," Finite Elem. Anal. Des. **47**(8), 906-912 (2011).
[10] H. H. Hu, D. D. Joseph, and M. J. Crochet, "Direct simulation of fluid particle motions," Theor. Comput. Fluid Dyn. **3**(5), 285 (1992).
[11] H. H. Hu, N. A. Patankar, and M. Y. Zhu, "Direct numerical simulations of fluid-solid systems using the arbitrary Lagrangian-Eulerian technique," J. Comput. Phys. **169**, 427-462 (2001).
[12] M. Coquerelle and G. Cottet, "A vortex level set method for the two-way coupling of an incompressible fluid with colliding rigid bodies," J. Comput. Phys. **227**(21), 9121-9137 (2008).
[13] R. Glowinski, T. W. Pan, T. I. Hesla, and D. D. Joseph, "A distributed Lagrange multiplier/fictitious domain method for particulate flows," Int. J. Multiphase Flow **24**, 755-794 (1999).
[14] N. A. Patankar, P. Singh, D. D. Joseph, R. Glowinski, and T. W. Pan, "A new formulation of the distributed Lagrange multiplier/fictitious domain method for particulate flows," Int. J. Multiphase Flow **26**, 1509-1524 (2000).
[15] R. Glowinski, T. W. Pan, T. I. Hesla, D. D. Joseph, and J. Pĕriauxz, "A fictitious domain approach to the direct numerical simulation of incompressible viscous flow past moving rigid bodies: Application to particulate flows," J. Comput. Phys. **169**, 363-426 (2001).
[16] T. Lee, Y. Chang, J. Choi, D. Kim, W. Liu, and Y. Kim, "Immersed finite element method for rigid body motions in the incompressible Navier-Stokes flow," Comput. Methods Appl. Mech. Eng. **197**, 2305-2316 (2008).
[17] S. Ghosha and J. M. Stockiea, "Numerical simulations of particle sedimentation using the immersed boundary method," Commun. Comput. Phys. **18**, 380-416 (2015).
[18] J. Zhao, "Aerodynamics of seed dispersal," Ph.D. thesis, New York University, 2011.
[19] M. Uhlmann, "An immersed boundary method with direct forcing for the simulation of particulate flows," J. Comput. Phys. **209**, 448-476 (2005).
[20] S.-W. Su, M.-C. Lai, and C.-A. Lin, "An immersed boundary technique for simulating complex flows with rigid boundary," Comput. Fluids **36**, 313-324 (2007).
[21] W.-P. Breugem, "A second-order accurate immersed boundary method for fully resolved simulations of particle-laden flows," J. Comput. Phys. **231**, 4469-4498 (2012).
[22] R. D. Blevins, *Applied Fluid Dynamics Handbooks* (Van Nostrand Reinhold Company, 1984), pp. 279-381.
[23] A. Azuma and K. Yasuda, "Flight performance of rotary seeds," J. Theor. Biol. **138**, 23-34 (1989).
[24] M.-C. Lai and C. S. Peskin, "An immersed boundary method with formal second-order accuracy and reduced numerical viscosity," J. Comput. Phys. **160**, 705-719 (2000).
[25] D. M. McQueen and C. S. Peskin, "Heart simulation by an immersed boundary method with formal second-order accuracy and reduced numerical viscosity," in Mechanics for a New Millennium, Proceedings of the International Conference on Theoretical and Applied Mechanics (ICTAM) 2000.
[26] N. R. Clarke and O. R. Tutty, "Construction and validation of a discrete vortex method for the two-dimensional incompressible navier-stokes equations," Comput. Fluids **23**(6), 751-783 (1994).
[27] A. Fortes, D. D. Joseph, and T. S. Lundgren, "Nonlinear mechanics of fluidization of beds of spherical particles," J. Fluid Mech. **177**, 467-483 (1987).
[28] T. T. Bringley and C. S. Peskin, "Validation of a simple method for representing spheres and slender bodies in an immersed boundary method for Stokes flow on an unbounded domain," J. Comput. Phys. **227**, 5397-5425 (2008).
[29] R. Nathan, "Long-distance dispersal of plants," Science **313**, 786-788 (2006).
[30] D. Lentink, W. B. Dickson, J. L. van Leeuwen, and M. H. Dickinson, "Leading-edge vortices elevate lift of autorotating plant seeds," Science **324**, 1438-1440 (2009).
[31] A. Azuma, *The Biokinetics of Flying and Swimming*, AIAA Education Series (American Institute of Aeronautics & Astronautics, Reston, VA, 2006).
[32] K. Varshney, S. Chang, and Z. J. Wang, "The kinematics of falling maple seeds and the initial transition to a helical motion," Nonlinearity **25**, C1 (2012).
[33] B. E. Griffith, R. D. Hornung, D. M. McQueen, and C. S. Peskin, "An adaptive, formally second order accurate version of the immersed boundary method," J. Comput. Phys. **223**, 10-49 (2007).